Journal of the Korean Society of Surveying, Geodesy, Photogrammetry and Cartography
Vol. 34, No. 4, 391-402, 2016
http://dx.doi.org/10.7848/ksgpc.2016.34.4.391

ISSN 1598-4850(Print)
ISSN 2288-260X(Online)
Original article

A Similarity Weight-based Method to Detect Damage Induced by a Tsunami

Jeon, Hyeong-Joo[1] · Kim, Yong-Hyun[2] · Kim, Yong-Il[3]

Abstract

Among the various remote sensing sensors compared to the electro-optical sensors, SAR (Synthetic Aperture Radar) is very suitable for assessing damaged areas induced by disaster events owing to its all-weather day and night acquisition capability and sensitivity to geometric variables. The conventional CD (Change Detection) method that uses two-date data is typically used for mapping damage over extensive areas in a short time, but because data from only two dates are used, the information used in the conventional CD is limited. In this paper, we propose a novel CD method that is extended to use data consisting of two pre-disaster SAR data and one post-disaster SAR data. The proposed CD method detects changes by using a similarity weight image derived from the neighborhood information of a pixel in the data from the three dates. We conducted an experiment using three single polarization ALOS PALSAR (Advanced Land Observing Satellite/Phased Array Type L-Band) data collected over Miyagi, Japan which was seriously damaged by the 2011 east Japan tsunami. The results demonstrated that the mapping accuracy for damaged areas can be improved by about 26% with an increase of the g-mean compared to the conventional CD method. These improved results prove the performance of our proposed CD method and show that the proposed CD method is more suitable than the conventional CD method for detecting damaged areas induced by disaster.

Keywords : SAR, Change Detection, Similarity Weight Image, Damage Assessment

1. Introduction

The frequency of natural disasters has steadily increased in recent years (Hoyois *et al*., 2007), and large-scale disasters, such as tsunamis and earthquakes, have become very typical disasters. These large-scale disasters cause many casualties and extensive property damage over a wide area. Rapid observation after these catastrophic events is crucial for effective emergency response and decision making. In order to understand the damage situation over wide areas in a short span, remote sensing with extensive spatial coverage has played an important role.

Among the various sensors used in remote sensing, high-resolution optical images have typically been used to detect damaged areas (Adams *et al*., 2004; Saito *et al*., 2004). However, optical images are affected by weather conditions and illumination. In contrast to optical sensors, a SAR (Synthetic Aperture Radar) is an active sensor that functions independently of illumination and weather conditions, and this makes it useful for disaster monitoring. A number of studies using SAR images for tsunami damage assessment have been reported (Chini *et al*., 2012; Liu *et al*., 2012; Gokon *et al*., 2014; Dumitru *et al*., 2015). In these studies, full polarimetric SAR images were mainly used to detect damage induced by tsunamis in recent years (Watanabe *et al*., 2012; Chen and Sato, 2013; Park *et al*., 2013), and the authors reported that single polarization SAR images limit the information describing land surface compared to full

Received 2016. 07. 22, Revised 2016. 08. 05, Accepted 2016. 08. 15
1) Member, Dept. of Civil and Environmental Engineering, Seoul National University (E-mail: imsognatori@snu.ac.kr)
2) Member, Dept. of Civil and Environmental Engineering, Seoul National University (E-mail: yhkeen@gmail.com)
3) Corresponding Author, Member, Dept. of Civil and Environmental Engineering, Seoul National University (E-mail: yik@snu.ac.kr)

polarimetric SAR images. However, a single polarization SAR image can cover a wider area than a full polarimetric SAR image (Ainsworth *et al*., 2009), making it suitable for assessing damage induced by large-scale natural disasters.

Single polarization SAR images have been extensively used for the assessment of damage caused by large-scale disasters (Yonezawa and Takeuchi, 2001; Matsuoka and Yamazaki, 2004; Matsuoka and Yamazaki, 2005; Arciniegas *et al*., 2007; Bovolo and Bruzzone, 2007; Brunner *et al*., 2010; Chini *et al*., 2012; Jung and Kim, 2016). Arciniegas *et al*. (2007) and Chini *et al*. (2012) utilized the complex coherence of the interferometric pair for damage assessment. Matsuoka and Yamazaki (2004), Matsuoka and Yamazaki (2005), and Yonezawa and Takeuchi (2001) proposed methods that used intensity changes and intensity correlation to detect damage. Jung and Kim (2016) also used intensity changes and textual features to assess damage. Brunners *et al*. (2010) detected the damaged areas using the similarity between a simulated image and an actual SAR image that was generated by using optical and SAR images. Most of these studies utilized a CD (Change Detection) method that incorporated a DI (Difference Image) made from data of only two dates (one pre-disaster, one post-disaster data), to detect a change in areas (Bovolo and Bruzzone, 2007). Although multitemporal SAR data provides more information about disasters (Bujor *et al*., 2004; Gamba *et al*., 2007), the conventional CD methods utilize only two dates, which limits the information that can be provided.

In this paper, we propose a novel CD method using a similarity weight image that is extended to use data from three dates, comprising two pre-disaster SAR images and one post-disaster SAR image, for detecting a damaged area. The similarity weight image used in the proposed CD method is generated by a similarity weight derived from the neighborhood information of a pixel in the data of the three dates. Our experimental results confirmed that the similarity weight image reduces speckle noise and increases the mapping accuracy of damaged areas when compared to the DI used in the conventional CD method. For the experiment, we used three single polarization ALOS/PALSAR (Advanced Land Observing Satellite/Phased Array Type L-Band SAR) images on a subset of Miyagi prefecture, Japan, which was seriously damaged by a tsunami on March 11, 2011. This paper is organized as follows: In Section 2, the proposed method is described in detail; in Section 3, we describe the datasets, results, and discussion; conclusions are drawn in Section 4.

2. Methodology

We consider three co-registered SAR images I_1, I_2, and I_3 with M×N size and acquired over the same area at different times t_1, t_2, and t_3, respectively. Here, t_1 and t_2

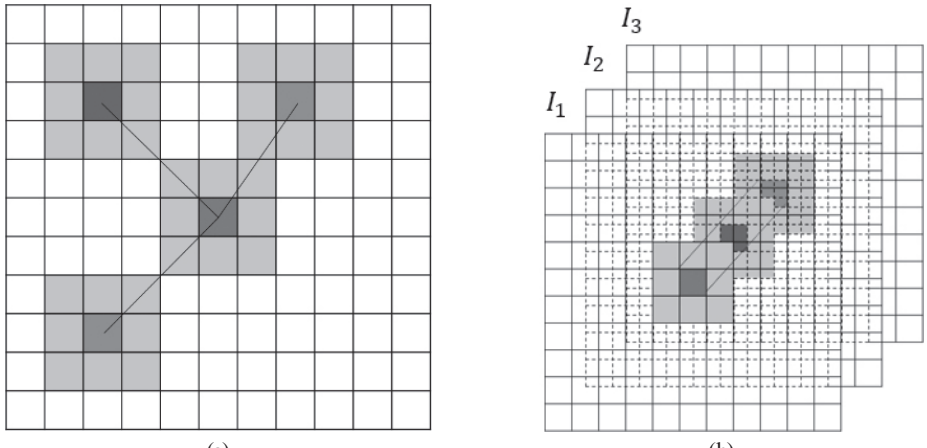

Fig. 1. Concept of similarity weight: (a) conventional similarity weight and (b) transformed similarity weight (gray: neighborhood pixel; red, blue, and green: center pixel)

are the pre-disaster time, and t_3 is the post-disaster time. Our objective is to produce a change-detection map, which represents changes that were induced by tsunamis, by using three images that consist of two pre-disaster images (I_1 , I_2) and one post-disaster image (I_3). The proposed approach consists of two main steps: 1) a similarity weight image for CD; 2) a threshold selection process. The first step uses three SAR images to estimate a similarity weight by utilizing the similarity weight equation used in a NL-means (Non-Local means) algorithm. In the second step, threshold selection is applied to identify tsunami-induced damaged areas. The details of the methodology are described below.

2.1 Similarity weight image for change detection

An NL-means algorithm is a denoising algorithm that reduces speckle noise. Denoising is achieved by averaging pixel values weighted by the similarity of neighborhoods of each pixel in an image (Tasdizen, 2009). The conventional similarity weight is a degree of the similarity between neighborhoods of each pixel in an image (Yousif and Ban, 2014). Fig. 1(a) shows that the conventional similarity weight is estimated by calculating the similarity between two square neighborhoods of fixed size and centered at a pixel in an image. In other words, the similarity weight between two square neighborhoods of two pixels (a blue pixel and a red pixel) means how similar to a square neighborhoods of a pixel (a blue pixel) compared to the other pixels (green pixels) on basis of a square neighborhoods of a pixel (a red pixel). We apply the similarity weight to detect damaged areas induced by a tsunami. In this paper, the similarity weight is transformed into a degree of the similarity between image neighborhoods of each pixel in three images (Fig. 1(b)). The transformed similarity weight w_{ij}^{pg} in a (p, q) pixel is expressed as Eq. (1) and Z is the normalizing constant and defined as Eq. (2).

$$w_{ij}^{pq} = \frac{1}{Z}\exp\left(\frac{|X_i - X_j|^2}{h^2}\right) \quad (1)$$

$$Z = \sum_j \exp\left(\frac{|X_i - X_j|^2}{h^2}\right) \quad (2)$$

Here, $X_i\,[i \in (1,2)]$ is a feature vector that consists of all values in the neighborhood of a pixel located in (p, q) of image I_i, which is a base image; X_j $\{j \in [\, i \neq j,\ j \in (1,2,3)]\}$ is a feature vector that consists of all values in the neighborhood of a pixel located in (p, q) of image I_j; and parameter h controls the decay of the exponential function. In Yousif and Ban (2014), the SAR ratio image, which applied an NL-means algorithm, is logarithmically transformed in order to meet the basic assumption in an NL-means algorithm (i.e., additive noise). Accordingly, we also transformed SAR images logarithmically.

In this paper, we define a similarity weight image (W_i) as a similarity weight between two pre-disaster images, and assume that the difference value in neighborhoods around a same-located pixel is small between two pre-disaster images. Accordingly, as there are many changes in a damaged area after a disaster, the similarity weight indicates a high value. In addition, a base image should be one of two pre-disaster images, and two similarity weight images (W_1 , W_2) are generated by each w_{12}^{pg}, w_{21}^{pg} . The proposed method uses two similarity weight images (W_1 , W_2) to detect damage induced by tsunamis.

2.2 Threshold selection process

To identify tsunami-induced changes, it is necessary to set a threshold of the similarity weight for discriminating changed and unchanged classes. A CD map is computed by assigning pixels to one class (changed, 1; unchanged, 0) according to a threshold T. The CD map (M_i) on a similarity weight image (W_i) is expressed as Eq. (3).

$$M_i = \begin{cases} 1 & if, W_i > T \\ 0 & if, W_i \leq T \end{cases} \quad (3)$$

Here, M_i is a binary image, and T is the threshold value supplied manually or automatically (Bovolo and Bruzzone, 2008). In this paper, we automatically select the threshold value. We assume Gaussian distribution due to the histogram of the similarity. Thus, we apply the KI (Kittler and Illingworth) thresholding, which is a typical threshold method that assumes and applies the Gaussian distribution of the dataset, to the similarity weight image (Kittler and Illingworth, 1986).

Before applying the threshold selection process, we mask the areas that do not meet the assumptions in the proposed method. The areas indicate regions where there are many

changes between two pre-disaster images and are mainly composed of vegetation areas which are sensitive to seasonal weather. In this case, we are unable to judge whether the changes are induced by tsunamis or seasonal effects, and so we consider them unreliable in terms of tsunami-induced changes when using intensity or amplitude SAR images. The process of generating a masking file consists of three steps. The first step generates the log ratio image of two pre-disaster images (I_1, I_2). In the second step, the KI threshold method is applied to the log ratio image. Finally, a MRF (Markov Random Field), which is a powerful tool for modelling contextual information, is applied to reduce the effect of speckle noise. After masking, the threshold selection process is applied to the masked similarity weight images. Then, two CD maps (M_1 , M_2) are generated from two similarity weight image (W_1 , W_2). The whole process is presented in Fig. 2.

For comparison, two log ratio image (R_1, R_2) are used, in which one (R_1) is generated from two images (I_1 , I_3) and the other (R_2) is generated from two images (I_2, I_3), by using a log ratio operator which is the most widely used operator to generate a DI. Next, masking is applied to each log ratio by using the masking file. Finally, two CD maps (r_1 , r_2) are generated by applying the same thresholding method that is applied to the similarity weight image for comparison with M_1 , M_2 .

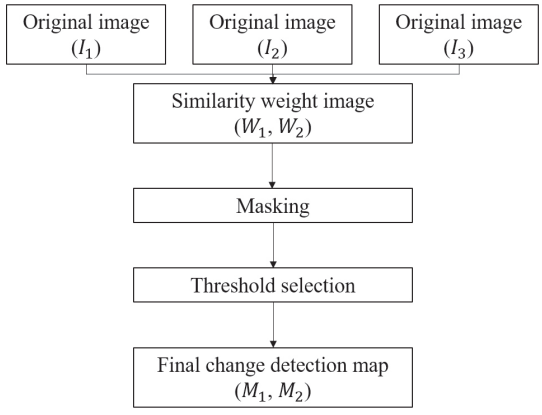

Fig. 2. Flowchart of the proposed change detection method

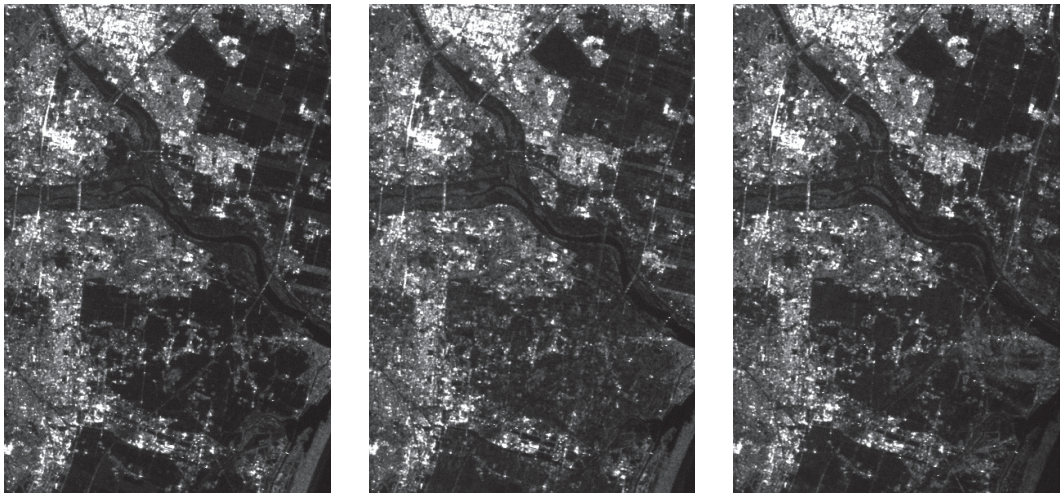

(a) (b) (c)

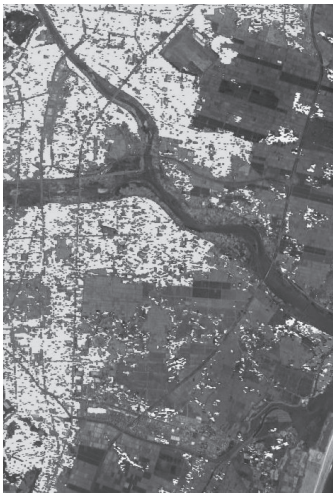

(d)

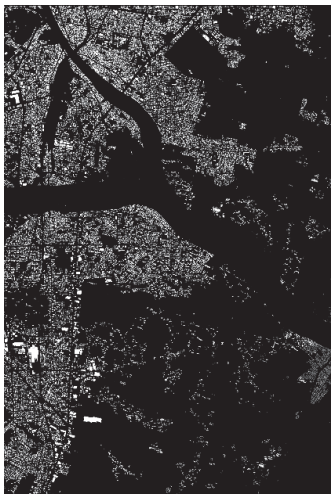

(e)

Fig. 3. ALOS/PALSAR amplitude images: (a) Pre-disaster (2010.05.20), (b) pre-disaster (2010.11.20), (c) post-disaster (2011.04.07), (d) building damage map, and (e) reference map

3. Experimental Results

3.1 Study area and datasets

The study site is Miyagi prefecture located on the Pacific coast of northern Japan. Miyagi prefecture was one of the areas most seriously damaged by the great tsunami on March 11, 2011. Most of the houses collapsed or were submerged. The building damage map is shown in Fig. 3(d), which was produced by the GIS (Geographic Information System) Center for Environment and Disaster Mitigation, Niigata University (http://www.jsgi-map.org/tsunami/). The building damage map is made up of four color types: red and pink are the collapsed buildings, yellow is the submerged buildings, purple is unknown, and green is undamaged buildings. We used only the collapsed buildings to evaluate the accuracy of the proposed method because the effect of the submerged buildings might be small in intensity or amplitude in a post-disaster SAR image on April 07, 2011. The reference map contains 168,543 unchanged pixels and 5,459 changed pixels; and is generated through three steps. The first step transforms the KML file into a shape file by using the ArcGIS program. In the second step, the reference map is generated from the shape file by using the ENVI (Exelis Visual Information Solutions) program. Finally, in order to improve the accuracy of the reference map, the reference map is registered to a SAR image through the ENVI program (Fig. 3(e)).

The datasets used in this paper consist of three images (Fig. 3): two ALOS/PALSAR images acquired before the tsunami on May 20, 2010, and November 20, 2010, as pre-disaster images (Fig. 3(a) and (b)) and one ALOS/PALSAR

Table 1. Acquisition information of datasets

Acquisition mode	Acquisition date	Polarization	Incidence angle [°]
FBS	May 20, 2010 (pre-disaster)	HH	38
FBS	November 20, 2010 (pre-disaster)	HH	38
FBS	April 07, 2011 (post-disaster)	HH	38

* FBS: Fine Beam Single Polarization mode

image acquired after the tsunami on April 07, 2011, as a post-disaster image (Fig. 3(c)). All images were geocoded and accurately co-registered to each other by the SNAP (Sentinel Application Platform). The spatial resolution of all SAR images was 7m, and the size of all images was 1500×1000 pixels. After co-registering, all SAR images were filtered by an enhanced Lee filter with a –5×5-sized window, which has proved effective in reducing speckle noise (Lopes *et al*., 1990). The acquisition information of the datasets used (acquisition date, polarization, incidence angle) is presented in Table 1. All images were taken on a descending orbit mode.

3.2 Results and discussion

In this section, we present detailed experimental results studying the behavior of the CD algorithm with respect to parameter h , the neighborhood size, and threshold selection. We also present a quantitative analysis of the results. In the quantitative analysis, false alarms (i.e., unchanged pixels wrongly classified as changed), missed alarms (i.e., changed pixels wrongly classified as unchanged), detected changes (i.e., changed pixels correctly classified as changed), overall accuracy (i.e., false alarms and missed alarms), and a g-mean (Kubat *et al*., 1998) are used to evaluate an effectiveness of the proposed method. The g-mean is measured by the accuracy rate of both the damaged and undamaged areas. The details are described below.

3.2.1 Interpretation of similarity weight image

A similarity weight image that was generated by using two pre-disaster images and one post-disaster image is used to detect damage induced by tsunamis through Eq. (1). Similarity values indicate the following: a low similarity weight means a base image is more similar to a post-disaster image than to the other pre-disaster image; a medium similarity weight indicates all three images are similar; and a high similarity weight means that the post-disaster image is very different than the two pre-disaster images. In Fig. 4(b), one can observe that the high similarity weights are mainly distributed near the shoreline where there are many damaged areas (Fig. 4(b), black rectangle), medium similarity weights are mainly distributed in areas away from the shoreline where there are many undamaged areas (Fig. 4(b), dot-dashed white square), and low similarity weights are mainly distributed in vegetation areas (Fig. 4(b), dotted white square).

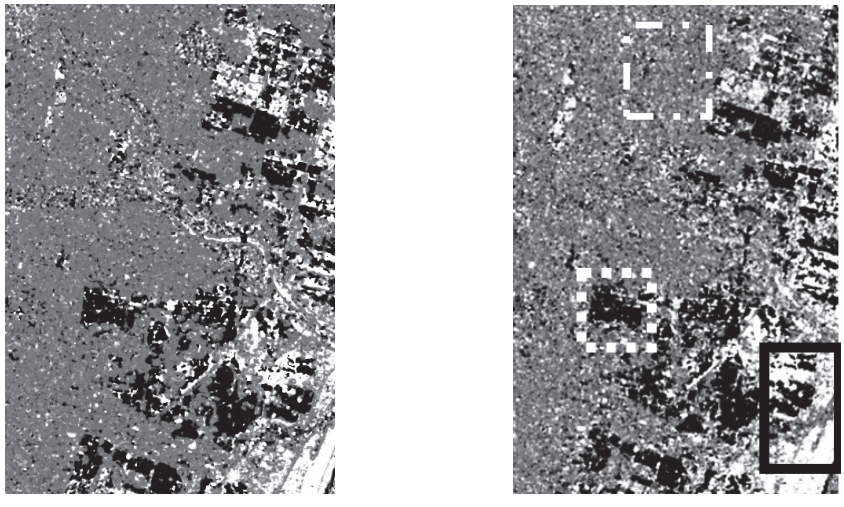

(a) (b)

Fig. 4. Similarity weight images versus h: (a) similarity weight image in $h = 10 \times \sigma_n$ and (b) similarity weight image in $h = 1$ (σ_n is a standard deviation in a neighborhood window) (balck rectangle: high similarity weight, dotted white square: low similarity weight, dot-dashed white square: medium similarity weight)

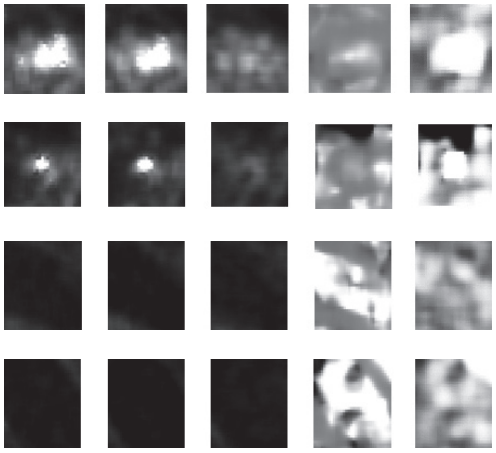

Fig. 5. The effect of parameter *h*: (a) hetero-case 1, (b) hetero-case 2, (c) homo-case 1, and (d) homo-case 2 (the first column is a patch of an image on May 20, 2010, the second on November 20, 2010, the third on April 07, 2011, the fourth on similarity weight image in $h = 10\times\sigma_n$, the fifth on similarity weight image in $h = 1$)

The similarity weight depends on the parameter *h*. Buades *et al*. (2005), who developed an NL-means algorithm, proposed that the value of *h* can be determined by using $h = 10\times\sigma_n$, which is subjective (Yousif and Ban, 2013). Fig. 4(a) is the similarity weight image in which *h* is set to $10\times\sigma_n$. With this setting, small changed areas in all three images are considered as large changed areas (i.e., high similarity weight) in homogeneous regions (Fig. 5(c) and (d)). On the other hand, in heterogeneous areas, large changed areas are considered as small changed areas (i.e., low similarity weight) (Fig. 5(a) and (b)). In other words, undamaged areas can be assigned as damaged areas in a homogeneous area, whereas damaged areas are assigned as unchanged areas in a heterogeneous area (fourth column in Fig. 5). This phenomenon is a problem when detecting damaged areas. For this reason, we empirically set *h* to a constant value 1. Fig. 4(b) is a similarity weight in which *h* is set to 1. The fifth column in Fig. 5 shows that the aforementioned problems are reduced.

3.2.2 Quantitative analysis of the results

In the first experiment, we analyzed the effect of masking in the similarity weight images. As mentioned in Section 2.2, it is necessary to mask the areas where there are many changes between two pre-disaster images before applying the thresholding method. To explore the effect of masking, the histograms of the masked similarity weight image were compared with those of the unmasked image in Fig. 6. The Fig. 6 shows that a portion of low similarity in the masked histogram is eliminated from the unmasked histogram. The remaining pixels were further analyzed to identify changed or unchanged pixels.

In the second experiment, we studied the similarity weight in terms of dependence on the neighborhood size of a pixel. When using a neighborhood window in SAR data, the neighborhood window size is influenced by the ENL (Equivalent Number of Looks) of the SAR data (Gong *et al*., 2012). A low ENL of the SAR data indicate a high noise level. In this case, a large neighborhood size is selected. In this paper, all ENL of the three SAR images are low, and we

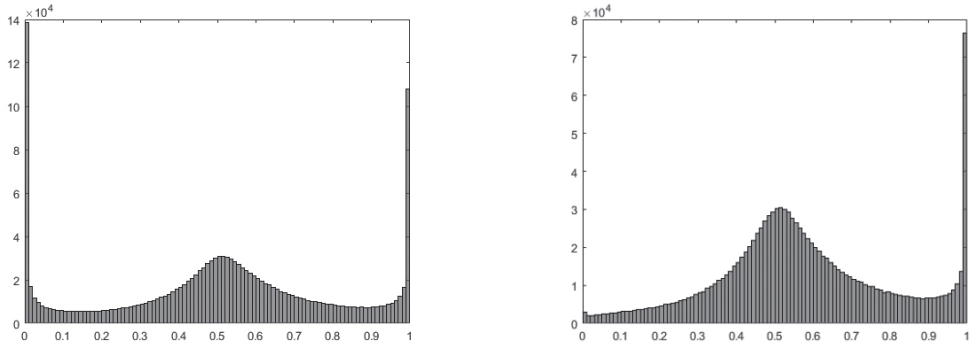

Fig. 6. Histograms of the similarity weight images before and after masking: (a) unmasked histogram and (b) masked histogram (x-axis, similarity weight; y-axis, number of pixels)

Table 2. False alarms, missed alarms, detected changes, overall accuracy, and g-means versus neighborhood size in M_1

M_1	False alarms	Missed alarms	Detected changes	Overall accuracy	G-mean (%)
3×3	5037	2739	2666	7776	41.3
5×5	3161	2723	2736	5884	48.2
7×7	1240	3371	2088	4611	49.0
9×9	2537	2286	3173	4823	56.8
11×11	4471	1505	3954	5976	58.3

Table 3. False alarms, missed alarms, detected changes, overall accuracy, and g-means versus neighborhood size in M_2

M_2	False alarms	Missed alarms	Detected changes	Overall accuracy	G-mean (%)
3×3	3284	2968	2491	6252	44.4
5×5	2570	2775	2684	5345	50.1
7×7	909	3616	1843	4525	47.5
9×9	1697	2641	2818	4338	56.7
11×11	2973	1737	3722	4710	61.6

speculate that the large neighborhood size is more effective than the small neighborhood size. In Table 2 and 3, false alarms, missed alarms, detected changes, overall accuracy, and g-means are shown versus the neighborhood size. We confirmed that the large neighborhood size is generally more suitable than the small neighborhood size. The proposed approach achieved the best performance with a neighborhood size of 11 × 11 pixels in two CD maps.

In the third experiment, we assessed the effectiveness of the proposed method through the comparison of two CD maps (r_1, r_2) that were made from each log ratio image (Fig. 7(b) and (c)). For accuracy, we used only collapsed buildings (Fig. 7(a)). Results are compared in Table 4, and the final CD maps are shown in Fig. 7. As reported in Table 4, we confirmed that the proposed method was improved when compared to r_1 and r_2 in all aspects (false alarms, missed alarms, detected changes, overall accuracy, and g-mean) for detecting damaged areas. The decreased number in false alarms means that the similarity weight image can reduce the negative effects of speckle noise when compared to the conventional DI. In Fig. 7(d) and (e), we can observe that the negative effects of speckle noise are shown to be reduced when compared to two CD maps made from the conventional DI. In terms of g-means, the similarity weight image was improved 20.4-26.4% compared to the conventional DI.

Table 4. Results achieved by the proposed method and the conventional method

	False alarms	Missed alarms	Detected changes	Overall accuracy	G-mean (%)
M_1	4471	1505	3954	5976	58.3
M_2	2973	1737	3722	4710	61.6
r_1	4373	3371	2088	7744	35.2
r_2	4741	3101	2358	7842	37.9

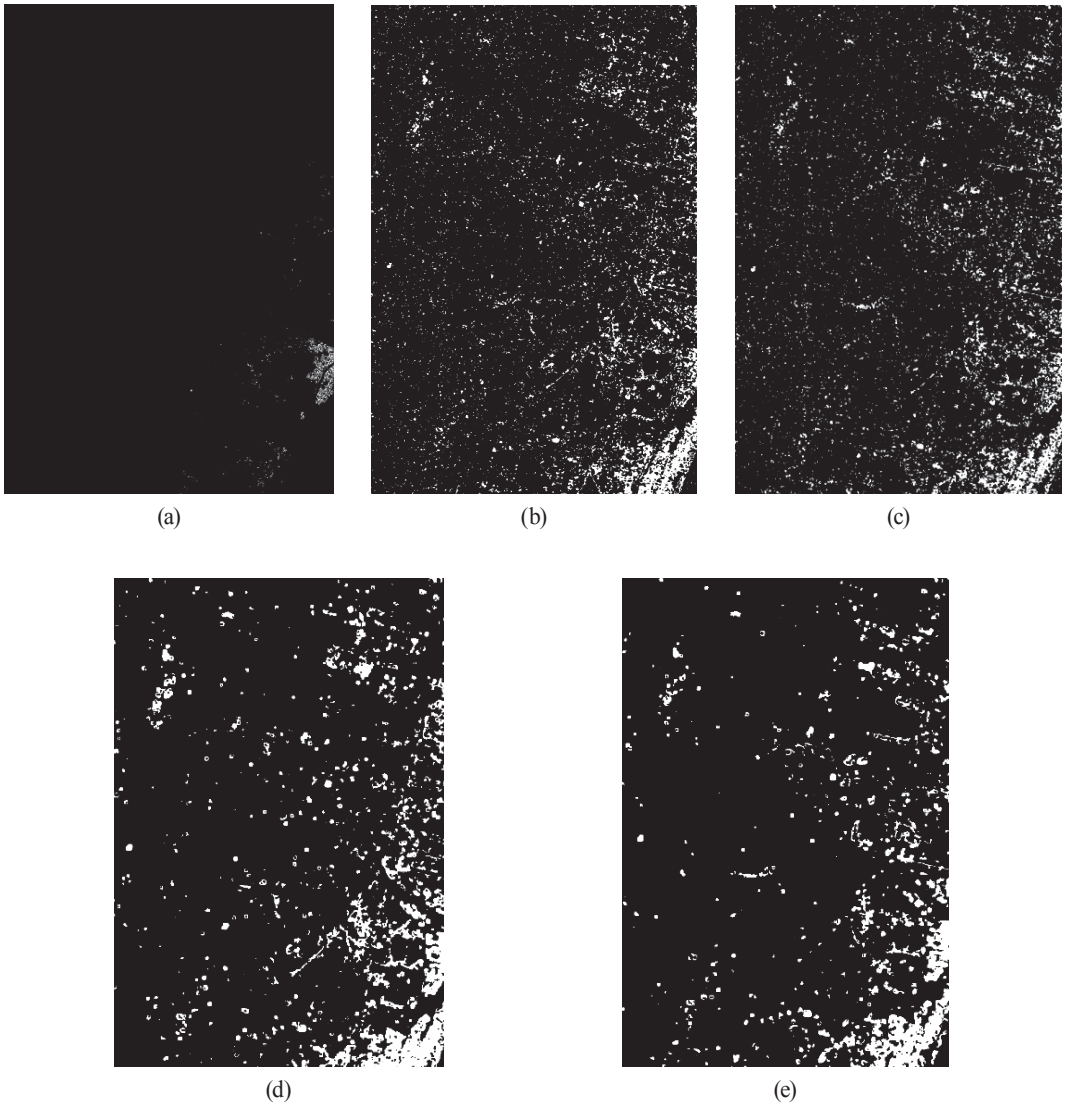

Fig. 7. Tsunami-induced change detection maps: (a) Reference map in terms of collapsed buildings, (b) r_1, (c) r_2, (d) M_1, and (e) M_2

Finally, we analyze the results in more details in terms of false alarms and missed alarms. Missed alarms consist of two types: The first type is caused when some changed areas between two pre-disaster images are incorrectly regarded as unchanged (Fig. 8); the second type is actual missed alarms. In this case, if the accuracy of the masking file is improved, the first type will be reduced. In Fig. 8, the first column is a patch of an image on May 20, 2010, the second was acquired on November 20, 2010, the third on April 07, 2011, and the fourth is a building, which is the first type of false alarm in the similarity weight image.

False alarms consist of three types: The first type is actual changed areas that are unchanged areas in the reference map (e.g. new building, changed land cover) (second and third row in Fig. 9); the second type is submerged areas with significant debris (first row in Fig. 9); the third type is actual false alarms. This is illustrated in Fig. 9, which is made up of Google Earth images and amplitude images. In Fig. 9, the first column is a

patch of an image on May 20, 2010, the second was acquired on November 20, 2010, the third on April 07, 2011, and the fourth is a building that is the first or second type of false alarm. The fifth is a Google Earth map on April 04, 2010, and the sixth is a Google Earth map on April 06, 2011. The first row is the second type, the second and third row are the first type.

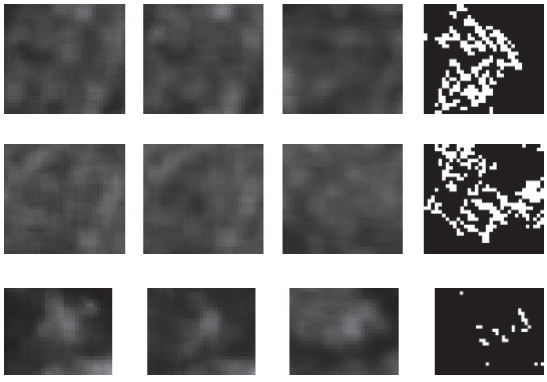

Fig. 8. Examples of the first type of missed alarms

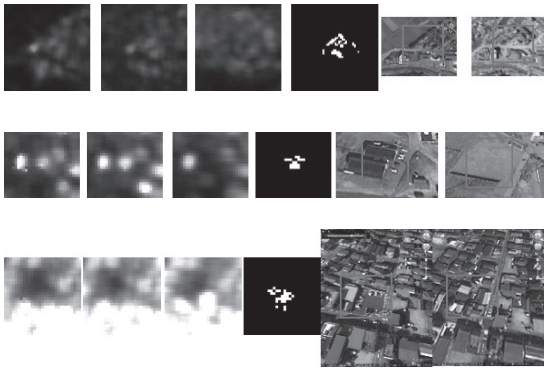

Fig. 9. Examples of the first and second type of false alarms

4. Conclusion

Remote sensing using satellite data has been growing in importance due to the steadily increasing number of natural disasters. Among various sensors used in remote sensing, the SAR sensor has been widely used for detecting damaged areas due to its insensitivity to illumination and weather conditions. Most studies using SAR images for CD apply a CD method using a DI, which is generated from data consisting of two dates. However, the conventional CD method is limited in that it uses the limited information provided from only two dates in multitemporal images.

In this paper, a novel CD method using a similarity weight image that is generated from three dates of SAR data has been presented for assessing changes induced by tsunamis. We confirmed the effectiveness of the similarity weight-based method, using three single polarization SAR images consisting of two pre-disaster SAR images and one post-disaster SAR image from Miyagi, Japan. We showed that the similarity weight-based method is effective for reducing the negative effect of noise when compared to the conventional CD method. Through a quantitative assessment of the results, we showed the usefulness of the proposed method for detecting damaged areas induced by tsunami. In future work, we plan to analyze the effect of parameter h when h is set to a different value considering various sites, and to analyze the distribution of the similarity weight image in more detail. In addition, we will extend a similarity image weight to apply to more than four images.

Acknowledgement

This research was supported by an NRF (National Research Foundation) grant funded by the South Korean Government (NRF-2014R1A1A1001995).

References

Adams, B.J., Huyck, C.K., Mansouri, B., Eguchi, R.T., and Shinozuka, M. (2004), *MCEER Research and Accomplishments 2003–2004*, A selection of papers chronicling technical achievements of the multidisciplinary center for earthquake engineering research, MCEER, New York, pp. 173-186.

Ainsworth, T.L., Kelly, J.P., and Lee, J.S. (2009), Classification comparisons between dual-pol, compact polarimetric and quad-pol SAR imagery, *ISPRS Journal of Photogrammetry and Remote Sensing*, Vol. 64, No. 5, pp. 464-471.

Arciniegas, G.A., Bijker, W., Kerle, N., and Tolpekin, V.A. (2007), Coherence-and amplitude-based analysis of seismogenic damage in Bam, Iran, using Envisat ASAR data, *IEEE Transactions on Geoscience and Remote Sensing*, Vol. 45, No. 6, pp. 1571-1581.

Bovolo, F. and Bruzzone, L. (2007), A split-based approach to unsupervised change detection in large-size multitemporal images: application to tsunami-damage assessment, *IEEE Transactions on Geoscience and Remote Sensing*, Vol. 45, No. 6, pp. 1658-1670.

Bovolo, F. and Bruzzone, L. (2008), An adaptive technique based on similarity measures for change detection in very high resolution SAR images, *IGARSS 2008-2008 IEEE International Geoscience and Remote Sensing Symposium*, IEEE, 7-11 July, Boston, United States of America, Vol. 3, pp. 158-161.

Brunner, D., Lemoine, G., and Bruzzone, L. (2010), Earthquake damage assessment of buildings using VHR optical and SAR imagery, *IEEE Transactions on Geoscience and Remote Sensing*, Vol. 48, No. 5, pp. 2403-2420.

Buades, A., Coll, B., and Morel, J.M. (2005), A non-local algorithm for image denoising, *IEEE Computer Society Conference on Computer Vision and Pattern Recognition*, IEEE, 20-25 June, San Diego, United States of America, Vol. 2, pp. 60-65.

Bujor, F., Trouvé, E., Valet, L., Nicolas, J.M., and Rudant, J.P. (2004), Application of log-cumulants to the detection of spatiotemporal discontinuities in multitemporal SAR images, *IEEE Transactions on Geoscience and Remote Sensing*, Vol. 42, No. 10, pp. 2073-2084.

Chen, S.W. and Sato, M. (2013), Tsunami damage investigation of built-up areas using multitemporal spaceborne full polarimetric SAR images, *IEEE Transactions on Geoscience and Remote Sensing*, Vol. 51, No. 4, pp. 1985-1997.

Chini, M., Pulvirenti, L., and Pierdicca, N. (2012), Analysis and interpretation of the COSMO-SkyMed observations of the 2011 Japan tsunami, *IEEE Geoscience and Remote Sensing Letters*, Vol. 9, No. 3, pp. 467-471.

Dumitru, C.O., Cui, S., Faur, D., and Datcu, M. (2015), Data analytics for rapid mapping: case study of a flooding event in Germany and the tsunami in Japan using very high resolution SAR images, *IEEE Journal of Selected Topics in Applied Earth Observations and Remote Sensing*, Vol. 8, No. 1, pp. 114-129.

Gamba, P., Dell'Acqua, F., and Trianni, G. (2007), Rapid damage detection in the Bam area using multitemporal SAR and exploiting ancillary data, *IEEE Transactions on Geoscience and Remote Sensing*, Vol. 45, No. 6, pp. 1582-1589.

Gokon, H., Koshimura, S., Post, J., Geiß, C., Stein, E., and Matsuoka, M. (2014), Detecting building damage caused by the 2011 Tohoku earthquake tsunami using TerraSAR-X data, In *2014 IEEE Geoscience and Remote Sensing Symposium*, IEEE, 13-18 July, Quebec, Canada, pp. 1851-1854.

Gong, M., Cao, Y., and Wu, Q. (2012), A neighborhood-based ratio approach for change detection in SAR images, *IEEE Geoscience and Remote Sensing Letters*, Vol. 9, No. 2, pp. 307-311.

Hoyois, P., Scheuren, J.M., Below, R., and Guha-Sapir, D. (2007), *Annual Disaster Statistical Review: Numbers and Trends 2006*, The number and trends, Centre for research on the epidemiology of disasters, Brussels, p.48.

Jung, M.Y. and Kim, Y.I. (2016), Tsunami-induced change detection using SAR intensity and texture information based on the generalized Gaussian mixture model, *Journal of the Korean Society of Surveying, Geodesy, Photogrammetry and Cartography*, Vol. 34, No. 2, pp. 195-206.

Kittler, J. and Illingworth, J. (1986), Minimum error thresholding, *Pattern recognition,* Vol. 19, No. 1, pp. 41-47.

Kubat, M., Holte, R.C., and Matwin, S. (1998), Machine learning for the detection of oil spills in satellite radar images, *Machine learning*, Vol. 30, No. 2-3, pp. 195-215.

Liu, W., Yamazaki, F., Gokon, H., and Koshimura, S. (2012), Extraction of damaged buildings due to the 2011 Tohoku, Japan earthquake tsunami, *2012 IEEE International Geoscience and Remote Sensing Symposium*, IEEE, 22-27 July, Munich, Germany, pp. 4038-4041.

Lopes, A., Touzi, R., and Nezry, E. (1990), Adaptive speckle filters and scene heterogeneity, *IEEE Transactions on Geoscience and Remote Sensing*, Vol. 28, No. 6, pp. 992–

1000.

Matsuoka, M. and Yamazaki, F. (2004), Use of satellite SAR intensity imagery for detecting building areas damaged due to earthquakes, *Earthquake Spectra*, Vol. 20, No. 3, pp. 975-994.

Matsuoka, M. and Yamazaki, F. (2005), Building damage mapping of the 2003 Bam, Iran, earthquake using Envisat/ASAR intensity imagery, *Earthquake Spectra*, Vol. 21, No. S1, pp. 285-294.

Park, S.E., Yamaguchi, Y., and Kim, D.J. (2013), Polarimetric SAR remote sensing of the 2011 Tohoku earthquake using ALOS/PALSAR, *Remote Sensing of Environment*, Vol. 132, pp. 212-220.

Saito, K., Spence, R.J., Going, C., and Markus, M. (2004), Using high-resolution satellite images for post-earthquake building damage assessment: a study following the 26 January 2001 Gujarat earthquake, *Earthquake Spectra*, Vol. 20, No. 1, pp. 145-169.

Tasdizen, T. (2009), Principal neighborhood dictionaries for nonlocal means image denoising, *IEEE Transactions on Image Processing*, Vol. 18, No. 12, pp. 2649-2660.

Watanabe, M., Motohka, T., Miyagi, Y., Yonezawa, C., and Shimada, M. (2012), Analysis of urban areas affected by the 2011 off the Pacific coast of Tohoku earthquake and tsunami with L-band SAR full-polarimetric mode, *IEEE Geoscience and Remote Sensing Letters*, Vol. 9, No. 3, pp. 472-476.

Yonezawa, C. and Takeuchi, S. (2001), Decorrelation of SAR data by urban damages caused by the 1995 Hyogoken-nanbu earthquake, *International Journal of Remote Sensing*, Vol. 22, No. 8, pp. 1585-1600.

Yousif, O. and Ban, Y. (2013), Improving urban change detection from multitemporal SAR images using PCA-NLM, *IEEE Transactions on Geoscience and Remote Sensing*, Vol. 51, No. 4, pp. 2032-2041.

Yousif, O. and Ban, Y. (2014), Improving SAR-based urban change detection by combining MAP-MRF classifier and nonlocal means similarity weights, *IEEE Journal of Selected Topics in Applied Earth Observations and Remote Sensing*, Vol. 7, No. 10, pp. 4288-4300.